Progress in Additive Manufacturing
https://doi.org/10.1007/s40964-025-01275-2

RESEARCH

Microstructure formation during gas flow-assisted additive manufacturing of a metallic glass powder on ground and in microgravity

Melanie Clozel[1] · **Christian Neumann**[1] · **Johannes Thore**[1] · **Matthias Kolbe**[1] · **Fan Yang**[1] · **Olof Gutowski**[2] · **Ann-Christin Dippel**[2] · **Lucas M. Ruschel**[3] · **Ralf Busch**[3] · **Christoph Altenbach**[1] · **Chijioke Kenneth Akuata**[1,4] · **Daniela Zander**[1,4] · **Janka Wilbig**[5] · **Andreas Meyer**[1]

Received: 30 April 2025 / Accepted: 19 July 2025

Abstract

We studied bulk metallic glasses produced from gas flow-assisted laser-based powder bed fusion process, which is capable of additive manufacturing metallic parts in microgravity. A Zr-based bulk metallic glass composition $Zr_{59.3}Cu_{28.8}Al_{10.4}Nb_{1.5}$ has been processed on ground and in microgravity in a compact sounding rocket payload MARS-M. Microstructure characterization was performed using electron microscopy and X-ray diffraction computed tomography, which cope with small amounts of sample materials, especially for those fabricated under microgravity conditions. Very similar microstructures and crystalline fractions are observed in sample manufactured on ground and in microgravity, which shows that process parameters of conventional laser powder bed fusion for manufacturing metallic glasses can be transferred to the processes in microgravity. Two different origins of crystallization have been identified in the $Zr_{59.3}Cu_{28.8}Al_{10.4}Nb_{1.5}$ sample. The preferred occurrence of $CuZr_2$ at the interlayer boundaries is likely a result of recrystallization from the undercooled melt and hence associated with laser scanning strategy. In contrast, the more uniformly distributed Al_3Zr_4 phase is considered to be triggered by the formation of Cu_2Zr_4O. Thus, for the fabrication of fully amorphous builds both on ground and in space, our findings point to higher scanning speeds and lower oxygen contents, while the latter can also be used to tune the crystalline fractions in the sample.

Keywords Gas flow-assisted laser-based powder bed fusion · Microgravity · Glass-forming alloys · X-ray diffraction tomography

1 Introduction

Bulk metallic glasses (BMGs) are a relatively late arrival in the history of materials science, coming to existence in the early 1960s. Due to their amorphous structure and hence having no grain boundaries, they can display excellent corrosion resistance, good mechanical properties, and low friction coefficient, making them attractive for both ground and space applications [1, 2].

Generally produced by casting, the size of BMGs is usually limited to a few millimeters to centimeters in thickness due to dropping of cooling rates and therefore increased probabilities of crystallization when dimensions are increased during casting [3]. Optimization of the critical casting thickness of fully glassy samples, also known as glass forming ability (GFA), can be only achieved by delicate adjustment of the alloy composition. Recently, however, these materials have begun to be used in additive manufacturing (AM). By building layer by layer, it is possible to circumvent the usual size limitations and to form an amorphous part larger than that attained by casting [4–6].

Of all AM processes, laser-based powder bed fusion (LPBF) is one of the most versatile techniques due its range of possible geometries and scalable process parameters. It can be adapted to a wide range of materials [7–9], such as metals [4, 6, 10, 11], ceramics [12], and polymers [13, 14]. This makes it an attractive process for materials research as well as for industry. By now, this technology has become a reliable alternative for building structural parts [15] and parts with complex geometry or from materials difficult to handle in traditional ways [16].

Extended author information available on the last page of the article

AM technologies are considered as a necessity for space applications, particularly for exploration missions, because they contribute to saving material and reducing mass to transport as well as production time, allowing a fast and flexible response to the loss or damage of parts. However, the largest challenge in manufacturing parts in an LPBF process independent from gravity is the powder handling. On ground, the powder deposition relies on stabilization by gravity. It is, hence, necessary to compensate for lacking gravitational forces to use a powder bed under space conditions. One possibility is to use a gas flow-assisted powder deposition developed by Zocca et al. [17, 18], in which a porous build-platform is used in combination with a vacuum pump-driven reduced pressure. This creates a gas flow through the build-platform which stabilizes the powder. We have recently demonstrated that it is possible to produce BMG samples based on this gas flow-assisted powder handling system, using a compact additive manufacturing device MARS-M to perform LPBF onboard the DLR's MAPHEUS sounding rocket [19].

The combination of the gas flow-assisted powder deposition process and glass forming alloys introduces several aspects that differ from the conventional LPBF processes. The presence of a continuous gas flow might affect, e.g., heat transfer, pore formation, or impurities in the atmosphere. Bulk metallic glass forming alloy melts exhibit slow liquid dynamics, i.e., higher viscosity, more sluggish mass transport compared to that of the casting alloys. The sounding rocket payload is a Cartesian printer, which provide lower scanning speed compared to commercial printer on ground. Nevertheless, this means also prolonged time for phase and defect formations, particularly in the case of BMGs, which allows their origin to be studied in more details.

Therefore, in the following, we present a detailed examination of the parts produced in lab and in microgravity using the gas flow-assisted LPBF process for a BMG alloy composition widely used for AM, to understand mechanisms that control the microstructure formation during the process, as well as to evaluate the application perspective of the process on ground and under microgravity. The compositions studied here, $Zr_{59.3}Cu_{28.8}Al_{10.4}Nb_{1.5}$, have been considered as a possible material dedicated for efficient excavating tools during space exploration missions, owing to the excellent mechanical properties of BMGs, for which the relevant dimensions can be only manufactured additively [20]. The knowledge on these processes, in particular whether and how gravity affects the AM, allows to identify technologies with suitable materials and process conditions tailored for these applications.

Because the currently microgravity time available is limited, only a few layers can be produced under these conditions. Consequently, characterization techniques requiring only small amounts of material were chosen: scanning electron microscopy (SEM), transmission electron microscopy (TEM), as well as X-ray diffraction computed tomography at a synchrotron light source. With these, we show that gravity mainly affects the morphology of the print at large scale, on the order of millimeters, but not the microstructure and phase formation. In addition, with the spatial resolved diffraction technique, different origins of the crystalline phases have been identified.

2 Methods

2.1 Materials/alloys/powders

Powders of the metallic glass forming alloy AMLOY-Zr01 used in the current study ($Zr_{59.3}Cu_{28.8}Al_{10.4}Nb_{1.5}$ at.%, previously known as AMZ4) were purchased from Heraeus GmbH. The alloy is developed using a commercial grade Zr705 alloy, containing Nb, among other impurities, and is typically cheaper [21]. This also leads to an oxygen content of about 1 at.% in the alloy. The melt properties and crystallization behavior have been well studied. In particular, it has been shown that the amount of oxygen present does not affect the melt viscosity significantly, but lowers the degrees of undercooling and GFA [21, 22]. The powder was used at $15-45$ µm particle size, produced by inert gas atomization [23] and is amorphous, as determined by X-ray diffraction analysis (see Appendix A).

2.2 Additive manufacturing

All the additively manufactured samples were processed in the MARS-M sounding rocket payload [19]. A laser of 976 nm was used, with a maximum power of 283 W. The laser spot size is of about 80 µm. All samples were produced under (circulating) Ar atmosphere, with a residual O_2 content below 0.45%. The single-layer thickness was set to 100 µm. Samples were built on porous SS316L stainless steel build-platforms[1]. An overview of the lab and µg-samples investigated is listed in Table 1.

2.2.1 Sample printed on ground

A "twinline" scanning strategy was used on ground, which involves two alternating layers being displaced by half a hatch distance to each other [19]. This was found to increase density within the part (as determined by SEM observations). The scanning direction is also inverted for each new

---

[1] AISI 316 L/B, nominal composition: Cr 16.0-18.0 wt.%, Ni 10.0-14.0 wt.%, C $\leq$ 0.03 wt.%, Mo 2.0-3.0 wt.%, Fe balanced.

Table 1 Overview of the parameters used for the samples characterized in the current study

sample	laser power (W)	scanning speed (mm/min)	layers
Lab (parameter studies)	80	4000	20
	80	4750	20
	80	5500	20
	115	5500	20
	135	4000	20
	170	4000	20
	170	4750	20
	170	5500	20
flight sample	75	4000	8
lab equivalent	75	4000	8

layer, as this was found to reduce residual stress in the built, and hence preventing detaching of the part from the platform. The ground samples fabricated are 20 layers high, with a layer thickness of 100 µm and a hatch distance of 300 µm, which gives a sample cross-section of ~2×2 mm^2 (perpendicular to the laser scan direction). The laser power used covers a range from 55 to 195 W, while the scanning speed varies between 4000 and 5500 mm min^{-1} (a sample grid was manufactured with different laser power and scanning speeds, see Fig. 4 in Ref. [19]). The chosen range of parameters does not span the entire possibilities of the device, but is a reduced range within which the resulting samples can be processed for investigation (i.e., the powder is fully melted and the samples are sufficiently dense and do not shatter upon removal from the platform). The quality of these samples (density and crystallinity) was then investigated by SEM and X-ray diffraction analysis to determine the optimal applicable parameters.

2.2.2 Additive manufacturing under microgravity

Samples manufactured under microgravity conditions were processed in the MARS-M sounding rocket payload [19]. The MAPHEUS sounding rocket flight provides 6.5 min of microgravity. Thus, a sample with eight layers was fabricated, which provides enough material for analysis (see Fig. 1). It was built at 75 W and 4000 mm min^{-1}. The geometry is made of thin lines (single slugs) because of the requirements for the gas flow-assisted powder deposition: when a new layer is spread over the partly sintered powder bed, a low enough thickness of individual lines ensures that the powder is resting on top of it is maintained by the gas flow [24]. To study the influence of µg on the LPBF process, a lab equivalent sample was also built under the same conditions (same built geometry, process parameters, and built height).

Fig. 1 View of the flight sample built during the MAPHEUS-10 sounding rocket flight. The thickness of the sample is limited to eight-layers due to the available microgravity time of 6.5 min. The build is completely welded to the platform without detaching. The sample thickness mildly decreases toward the right half, due to feed-stock particle transport coming in from the left

2.3 Preparation steps for sample characterization

After building, the twinline samples processed on ground were either mechanically removed with pliers or left on the build-platform and cut into sections while still attached to the platform (as shown in Fig. 6). If the samples were meant for microscopy, they were then embedded in epoxy. The embedded samples were then ground and polished (final finishing with Buehler MicroCut® P4000, ChemoMet® polishing cloth, and MasterPrep™ suspension) to a mirror-like surface and examined using both optical microscopy and SEM. The samples used in the X-ray diffraction experiments were detached from the build-platform but not embedded.

In opposition to the ground samples, the µg-sample and its lab equivalent were left as-built as—due to the small thickness as well as the porosity of the build-platform—attempts to remove such samples from their platform proved detrimental to the integrity of the sample. The samples for Transmission Electron Microscopy (TEM) were prepared from the AMLOY-Zr01 µg-sample and its lab equivalent by means of Focused Ion Beam (FIB) using an FEI Strata 400 with Ga liquid metal ion source as well as a HELIOS dual beam with Xe plasma source. The macroscopic sampling site is the same single built-up segment of reticular structure marked by white arrows in Fig. 9. The two segments were cut free from the rest of the structure, followed by the preparation of an FIB lamella from each. The region of interest for FIB lift-out was located close to the interface between two layers at about half the height of the built-up structure. The dimensions of the FIB lamellae are ~17×4−7 μm (height × depth).

2.4 Electron microscopy

Scanning electron microscopy (SEM) was performed on a Zeiss Merlin Scanning Electron Microscope. The backscattered electron detector was used for all figures shown with energies ranging from 7 to 20 kV and a probe intensity of 2 nA. Energy-Dispersive X-ray Spectroscopy (EDS, Oxford Instruments) was performed for compositional analysis, while Electron Backscatter Diffraction (EBSD, Oxford Instruments) was performed for crystallographic analysis.

The near-interface microstructure of AMLOY-Zr01 samples was investigated by scanning transmission electron microscopy (S)TEM in bright-field (BF) mode using a JEOL JEM-F200 device operated at an acceleration voltage of 200 kV and equipped with a GATAN OneView camera for high-resolution imaging. The amorphousness was investigated by Selected Area Electron Diffraction (SAED) and high-resolution (HRTEM) imaging. HRTEM images of phases were processed by FFT and inverse FFT using ImageJ [25]. The resulting SAED-like diffraction patterns and lattice plane fringes enabled the identification of the phases. Additional information on the chemical composition of the phases was obtained in STEM mode by EDS using an Oxford Instruments detector. For both electron microscopy techniques, the preparation steps of the sample can be found in Sect. 2.3.

2.5 X-ray diffraction experiments

Both the X-ray micro-diffraction and the diffraction computed tomography (XRD-CT) focus primarily on the samples produced on ground, which have larger dimensions (cross-sections of about 2×2 mm^2 as mentioned above). X-ray micro-diffraction as well as diffraction tomography measurements were performed at the second experimental hutch (EH2) of the P07 High Energy Materials Science Beamline at DESY (Deutsches Elektronen-Synchrotron, Hamburg, Germany). For the micro-diffraction experiment scans were performed in transmission on detached ground samples along the build direction across a cross-section of 2×2 mm^2. An incoming X-ray energy of 103.5keV was used with a beam size of 2 μm (vertical) × 30 μm (horizontal). A DECTRIS PILATUS3 X CdTe 2 M area detector was placed at 348 mm downstream from the sample position, which gives an accessible momentum transfer q-range of $1-15$ Å^{-1}. The measurements were done in continuous scanning mode (at 2 s), with a sampling rate of 0.25s exposure time per diffraction image (4Hz), resulting in a covered scan range of 0.5 μm per image, and a spatial resolution on the sample of about 2.5 μm.

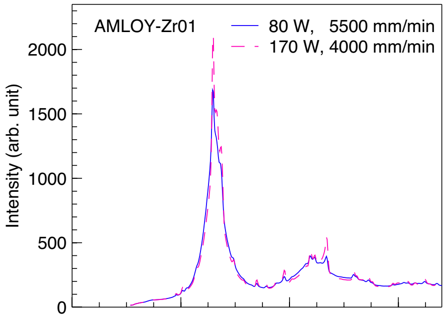

Fig. 2 Averaged X-ray micro-diffraction patterns of samples built with the lowest and highest energy density for AMLOY-Zr01

Figure 2 shows the average pattern over a whole sample for the samples with the highest and the lowest energy density as an example, confirming the crystalline phases visible in the X-ray micro-diffraction measurements.

In the case of XRD-CT measurements, the photon beam energy was reduced to 73.3 keV to have higher flux and detection efficiency. The beam size was 2 μm × 30 μm. A DECTRIS EIGER2 X CdTe 4 M detector was placed at a distance of 400 mm covering a usable q-range of 0.5 -8Å^{-1} running at 500 Hz (2 ms exposure time). The reconstructed datasets consist of 800 projections distributed over an angle of 360 deg. For each projection, a range of 3.6 mm was scanned across the sample in the direction perpendicular to the incoming beam with a constant speed of 1 mm s^{-1}. The resulting voxelsize is 2 μm × 2 μm.

The obtained 2D diffraction patterns were integrated to obtain 1D intensity profile using the pyFAI (Fast Azimuthal Integration using Python) software package [26]. For both experiments, integration parameters were obtained using CeO$_2$ calibrants. In the case of XRD-CT, the reconstruction was performed using a Matlab code developed at DESY.

2.6 Differential scanning calorimetry

Calorimetric experiments were performed using a power-compensated DSC8500 (PerkinElmer, USA). After equilibration at 303 K for 2 min, each sample was heated twice from 303 K to 853 K at heating rates of 0.33 K s^{-1}. The second run corresponds to the crystalline baseline, which was later subtracted from the first scan. The crystallization enthalpy was then determined by integrating the crystallization peak. The crystallization enthalpy release of casted, fully amorphous materials of AMLOY-Zr01 was used as a reference to estimate the amorphous fraction of the printed samples. The fully amorphous sample was produced by alloying high-purity elements (Zr, Cu, Al, Nb) in an arc-melter under high-purity Ar atmosphere, and subsequently suction casted into water-cooled copper mold. The casting dimensions were kept below the critical casting thickness. The amorphous nature of the casted sample was confirmed by XRD.

3 Results and discussion

3.1 Crystallinity

As already shown in the previous publication, the obtained samples were not fully amorphous [19], as can be also seen in Fig. 2. Compared to the additively manufactured AMLOY-Zr01 samples in the literature where fully amorphous print is achievable, the main reason for the partial crystallinity of the sample built in the MARS-M device is the limited scanning speed. The speeds recommended in the literature for AMLOY-Zr01 at 2000mm s^{-1} are at least an order of magnitude higher than what is attainable with MARS-M [23, 27, 28]. This is due to the mechanical and size requirements to the device for it to survive several rocket starts, re-entries, and landings. In view of long-term space applications, once the acceleration at launch will be reduced, higher scanning speeds are realizable without the necessity of a Cartesian setup.

Figure 3 shows the DSC scan curves of the printed and casted AMLOY-Zr01 samples. Samples were produced using two different laser powers: 80 W and 170 W. The laser scanning speed was kept constant at 4750 mm min^{-1}. Glass transition can be recognized as a small endothermic event, whereas crystallization events can be identified as large exothermic peaks. The characteristic temperatures and the obtained crystallization enthalpy are listed in Table 2.

Table 2 Characteristic temperatures and the crystallization enthalpy determined in the DSC measurements for the casted and printed AMLOY-Zr01 alloys

Sample	T_g (K)	T_x (K)	ΔH (Jg$^{-1)}$
AMLOY-Zr01			
as cast	661.9	741.0	63.37
80 W	664.7	745.8	43.73
170 W	663.3	751.3	39.43

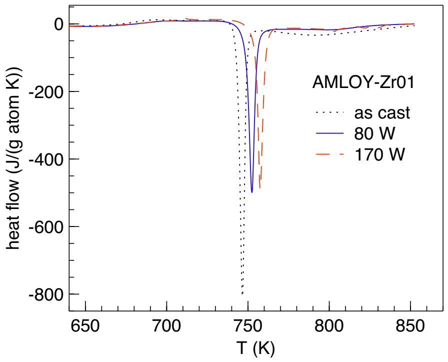

Fig. 3 DSC curves of as casted and printed samples of AMLOY-Zr01. For the printed samples, two different laser powers were used: 80 W and 170 W for each alloy. A scanning speed of 4750 mm min^{-1} was kept same for all samples, which also corresponds to the one used in the microgravity experiment. Positive values on the y-axis represent endothermic heat flow

The differential scanning calorimetry reveals a crystallization enthalpy of 3350 J mol^{-1}K^{-1} for the AMLOY-Zr01 sample printed with 80 W, 4750 mm min^{-1}, and 3020 J mol^{-1}K^{-1} for that printed with 170W, 4750 mm min^{-1}. This corresponds to an amorphous fraction of 69% and 62%, respectively, where the measured crystallization enthalpy of fully amorphous $Zr_{59.3}Cu_{28.8}Al_{10.4}Nb_{1.5}$ sample is 4854 J mol^{-1}K^{-1}. It seems that lower laser power at the same scanning speed results in less crystallization.

3.2 Distribution of amorphous and crystalline fractions

When looking at the variation in integrated peak intensity of the main Bragg peaks, a periodic repetition of the intensity maximum and minimum is observed, as shown in Fig. 4 for an AMLOY-Zr01 sample produced at four different process parameters (80 W, 4000 and 5500 mm min^{-1} as well as 80 W, 4000 and 5500 mm min^{-1}). An approximate 200 µm periodicity is obtained. On the crystallized AMLOY-Zr01 after annealing measured in the same micro-diffraction setup, this periodicity was no longer visible. Thus, this effect is not to be traced back to minor changes in sample thickness,

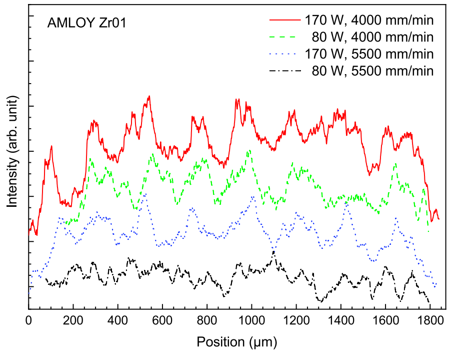

Fig. 4 Variation in the integrated intensity of the main Bragg peak for AMLOY-Zr01 (q-range between 2.56 and 2.64Å^{-1}) as the beam scans down the samples built at different processing parameters

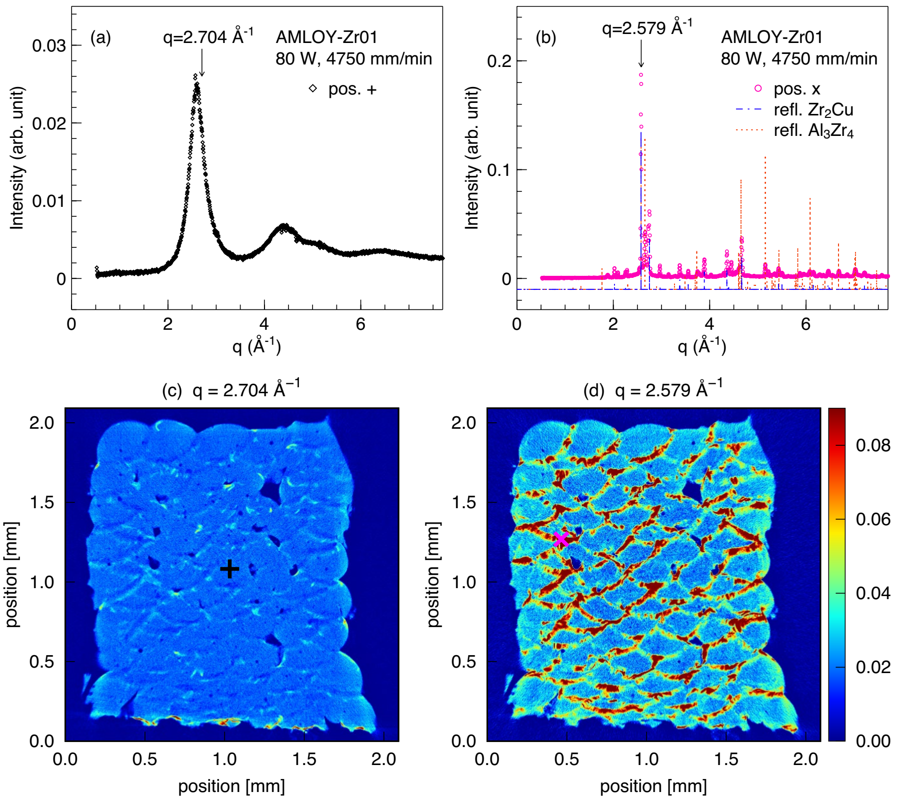

Fig. 5 XRD-CT of cross-sections of AMLOY-Zr01 built with 4750 mm min^{-1} and 80 W: (a) and (b) diffraction spectra at the positions shown in (c) and (d), respectively. Spectra are averaged over 9 pixels around the central position. (c) and (d) Intensity distribution over the entire sample at q-values corresponding to amorphous $q = 2.704\text{Å}^{-1}$ and crystalline material $q = 2.579\text{Å}^{-1}$. The brighter parts at the bottom of the sample in (c) stem from mixing with the steel platform, as shown later in Fig. 6. Intensity scales are kept same for both graphics

but indeed from changes in the ratio between the crystalline and the amorphous fractions at different build height in the sample.

This kind of periodicity in the patterns was observed for all the samples except the lowest energy density (i.e., 80 W, 5500 mm min^{-1}). Also, as shown in Fig. 2 and 4, the diffraction pattern and the integrated intensity do not show qualitative differences. Thus, it can be concluded that in process parameter range (laser power 80–170W, scan speed 4000 – 5500 mm min^{-1}), the crystalline phases formed do not show significant changes, at least for those measurable in the X-ray diffraction experiment. The observed intensity variation in Fig. 4 can be confirmed by SEM micrographs reported previously [19]. The periodicity would correspond to that of every two built layers, which can be understood in light of the developed scanning strategy, because odd-numbered layers are displaced by half a hatch distance (i.e., 150 µm) compared to even-numbered ones. However, both in X-ray micro-diffraction and in the SEM observations, also deviation from the 200 µm periodicity has been identified, indicating non-regular distribution of the crystalline fraction and layer boundaries in the sample.

As XRD-CT provides spatially resolved diffraction information, it is better suited to view these partially crystalline regions (non-destructively). Figure 5 shows the XRD-CT cross-sections and the corresponding diffraction patterns of the AMLOY-Zr01 sample built with a scanning speed of 4750 mm min^{-1} and a laser power of 80W. For each pixel (2 µm size), full diffraction information is available, as shown in Fig. 5a and b. For two q values 2.704Å^{-1} and 2.579Å^{-1}, intensity maps of the sample are shown in Fig. 5c and d. These two qs are chosen to resolve the spatial distribution of the amorphous and the crystalline phases: $q = 2.704\text{Å}^{-1}$ represents the amorphous region and is slightly above the position of the first structure factor maximum of the glass; $q = 2.579\text{Å}^{-1}$ corresponds to (103) and (111) Bragg reflections of the $CuZr_2$ and the Al_3Zr_4 phases, respectively[2], which are also later identified by SEM (Fig. 7), using particularly EBSD.

For the crystalline phases, the choice of the Bragg reflections is based on the consistently reported $CuZr_2$ and Al_3Zr_4 phases as the main crystallization products for additively manufactured AMLOY-Zr01 in the literature [29–34], with the presence of some Cu_2Zr_4O fractions. However, this choice of the representation does not exclude the potential presence of other crystalline phases in the sample. Nevertheless, identifying minor crystallization products is either beyond the capability of the spatial resolution of the XRD-CT configuration used here, or the

---

[2] Obtained by crystal structure analysis (Le Bail method using following crystalline structures: $CuZr_2$ *I4/mmm* with $a = 3.2315$ Å and $c = 11.1597$ Å, Al_3Zr_4 *P6/mmm* with $a = 5.4648$ Å and $c = 5.4051$ Å

positions of the Bragg peaks is rather close to those of the $CuZr_2$ and Al_3Zr_4 phases. The presence of other crystalline phases will be discussed together with the transmission electron microscopy results.

It can be seen that the intensity distribution is much more uniform in Fig. 5c (amorphous) compared to that in Fig. 5d (crystalline). This shows that the amorphous phase is present through out the sample, whereas the crystalline phases mainly appear in the regions between the layers. The curvature observed between the layers shows the contact geometry of the melt with the previous solidified track. The thickness of these boundary layers is estimated to be few tens of microns. The results confirm that the fraction of the crystalline phases is minor in the sample, as well as the observed irregularity of the ~200 µm periodicity in Fig. 4, as these interlayer boundaries are not aligned entirely parallel.

3.3 Influence of build-platform

In the MARS-M facility, the samples are manufactured onto a sintered porous SS316L stainless steel build-platform, and the first layer of the build is very much embedded and welded in this platform [19]. A cross-section of an as-built AMLOY-Zr01 sample ($5500\,\mathrm{mm\,min^{-1}}$ and 170 W) on the porous steel build-platform is shown in the left panel of Fig. 6.

When looking more closely at the sample-platform interface, mixing is visible, as shown in the right panel of Fig. 6. EDS analysis revealed some chemical mixing (see Table 3) and potentially formation of compositions, so far unidentified.

Since during processing of at least the first layer, the alloy melt is in contact with the platform, such a formation of new (e.g., iron containing) alloys can be expected. However, X-ray diffraction measurements reveal that such physical or chemical mixing is localized within the first, maximum the second layer (see diffraction pattern in Appendix Fig. B.1). It can also be seen from the XRD-CT images (Fig. 5c) that only a thin layer of a few tens of micron thickness at the bottom of the built sample shows a different diffraction pattern. This allows us to draw the conclusions that the stainless steel affects only a very limited region of the sample, and even in the flight samples with less layers, the majority part of the printed material has the same composition as of the powder.

3.4 Details and origin of the crystalline phases

In the following section, the details of the crystalline phases in the printed sample will be presented.

Figure 7a shows an SEM image of the crystalline regions of one powder layer including the boundaries areas to the upper and lower layers. It appears that the crystallization is of two types/steps. First, most of the crystal grains (dark areas in the image) are located in the interlayer region. These are known as the so-called heat-affected zones (HAZ) discussed in the literature [35–40], particularly from single track melting experiments on the AMLOY-Zr01 alloy [41]. This is a result of crystallization from undercooled melt where close to the laser heated area, the glassy materials

Table 3 Measured concentrations in at.% at different points of Fig. 6. The normial composition of the alloy is $Zr_{59.3}Cu_{28.8}Al_{10.4}Nb_{1.5}$. Cr and Ni are sourced from the base plate

Element	I	II	III	IV	V
O	11.75	13.71	13.96	7.12	5.13
Al	7.03	6.33	3.40	1.29	0.38
Cr	0.79	1.58	7.56	14.34	18.57
Fe	3.94	10.31	36.43	55.27	65.67
Ni	1.27	3.26	5.67	9.77	8.82
Cu	24.38	22.37	7.66	3.19	0.65
Zr	48.42	40.33	24.08	8.84	0.79
Nb	2.42	2.11	1.26	0.17	0

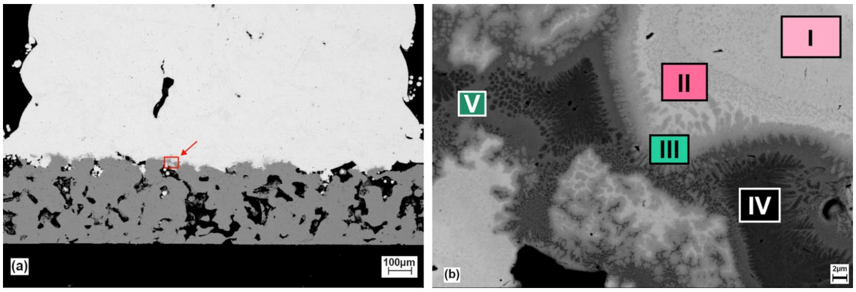

Fig. 6 (a) SEM micrograph of the cross-section of a "twinline" AMLOY-Zr01 sample as-built and still attached to the porous build-platform. The scale represents 100 µm. The arrow points to the location where a zoomed-in view was taken as shown in the right picture. (b) A closer look at the interface area, presenting different crystalline regions of varying compositions. The compositions determined by energy-dispersive X-ray analysis for each rectangle are presented in Table 3. The back-scattered electron detector was used. The scale bar represents 2 µm

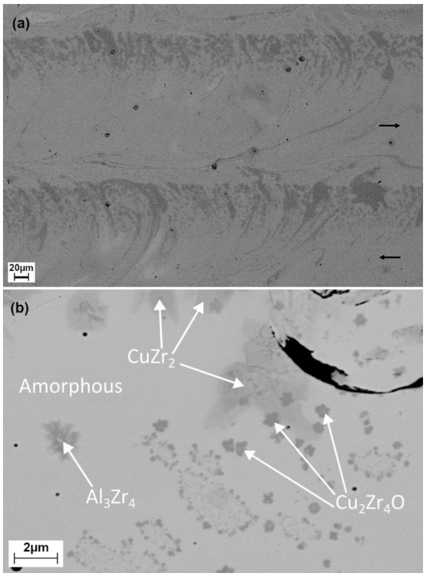

Fig. 7 (a) Increased magnification of a cross-section of AMLOY-Zr01 built with 4000 mm min^{-1} and 170W, parallel to the scanning direction. The scale represents 20 µm. The arrows indicate the scan direction in a single layer. (b) Various crystals appearing in AMLOY-Zr01 samples in the darker (crystalline) areas. The scale represents 2 µm. The crystals were identified thanks to EBSD

was heated above the glass transition. Second, some of the crystal grains have been displaced farther away from the layer interface. In this case, a more curvy morphology of the crystals can be observed. This indicates that these crystalline fractions are likely formed in the melt pool where convective flows are present, leading the crystals being displaced during or after formation.

Figure 7b shows the different type of crystal phases identified by SEM employing both EDS and EBSD analysis in the melt pool region. In particular, EBSD analysis using the Crystallographic Analysis of the Lattice Metric (CALM) software [42] revealed the presence of tetragonal CuZr$_2$, hexagonal Al$_3$Zr$_4$ and large cubic structure matched to Cu$_2$Zr$_4$O (CIF: 1220324, SG = 227, $a = 12.28$Å).[3] As industrial grade AMLOY-Zr01 powder was used, and the process gases contained additional oxygen contents, the presence of the Cu$_2$Zr$_4$O phase is expected, which has been shown to be stable at an oxygen concentration greater than 0.5 at.% [27]. The grain size of the observed Cu$_2$Zr$_4$O phase is typically below 1 µm, as shown in Fig. 7b. The typical grain size of the CuZr$_2$ and hexagonal Al$_3$Zr$_4$ are larger, but are mostly around or below 2 µm.

The observation of CuZr$_2$ and Al$_3$Zr$_4$ by SEM, particularly using EBSD, agrees with the XRD-CT results here. The Cu$_2$Zr$_4$O phase cannot be unambiguous identified in XRD-CT due to its small grain size and the overlapping Bragg reflections with other phases. The distributions of the CuZr$_2$ and Al$_3$Zr$_4$ in the bulk sample fabricated with 80W laser power and 4750 mm min^{-1} scanning speed are shown by the XRD-CT results (Fig. 8). Here, q values of 2.748 Å^{-1} and 2.649 Å^{-1} are chosen, which correspond to the CuZr$_2$ ((110) reflection) and the Al$_3$Zr$_4$ phases ((200) and (102) reflections), respectively, where the Bragg peaks are more separated from each other. The higher intensity between the lines and layers in Fig. 8a indicates that the CuZr$_2$ phase is more concentrated at the interface. In contrast, Al$_3$Zr$_4$ crystals are distributed more in the volume, which leads to higher intensities in the bulk, as well as at the outer edge of the sample. Although it should be noted that the overall intensity is lower compared to that for CuZr$_2$, indicating at

Fig. 8 XRD-CT of cross-sections of AMLOY-Zr01 built with 4750 mm min^{-1} and 80W at q-values corresponding to (a) CuZr$_2$ $q = 2.748$ Å^{-1} and (b) Al$_3$Zr$_4$ crystalline phases $q = 2.649$ Å^{-1}. Intensity scales are the same for both graphics

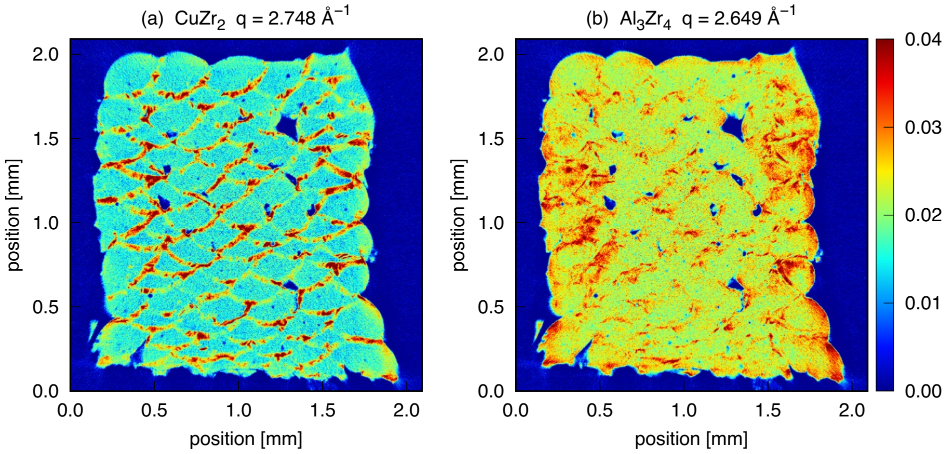

---

[3] crystal structure data from Pearson crystallographic database were used [P. Villars, K. Cenzual, Pearson's Crystal Data: Crystal Structure Database for Inorganic Compounds (on DVD), Release 2020/2021, ASM International®, Materials Park, Ohio, USA]

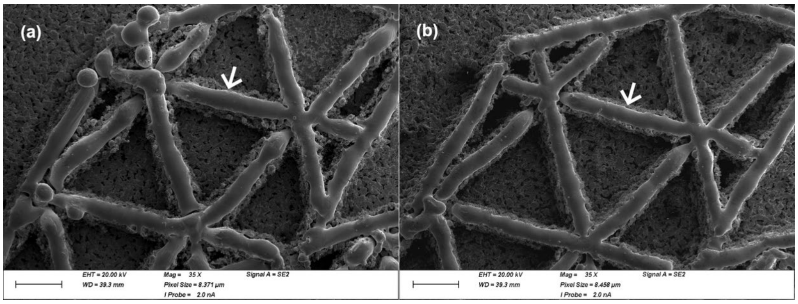

Fig. 9 SEM micrographs of the sample produced during the MAPHEUS-10 sounding rocket flight (a) and the equivalent lab sample (b). The background is the porous steel build-platform, as the samples were examined as-built. The scale represents 1 mm

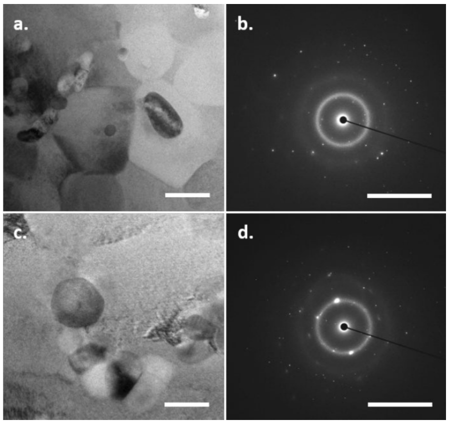

Fig. 10 TEM-BF images and the corresponding SAED patterns of MAPHEUS-10 µg-sample (a.-b.) and lab equivalent (c.-d.) near the interface of two layers. Scale bar of BF images (a., c.) is 100 nm and of SAED patterns (b., d.) 10 nm^{-1}

Table 4 Size of nanocrystalline spherical-shaped and ellipsoidal-shaped phases observed by TEM in µg-sample and lab equivalent of AMLOY-Zr01 in nm

	Flight Sample (nm)	Lab Equivalent (nm)
Spherical	21.12 ± 6.10	94.67 ± 25.62
Ellipsoidal		
Length	64.96 ± 20.86	113.40 ± 28.08
Width	33.70 ± 10.50	68.28 ± 16.86
Aspect Ratio	1.95 ± 0.34	1.70 ± 0.38

least qualitatively lower volume fraction of the Al_3Zr_4 phase. Taking into account the considerably higher melting point of Al_3Zr_4 compared to that of $CuZr_2$, it may be concluded that the Al_3Zr_4 phase is preferentially nucleated at higher temperatures and hence also earlier in the melt pool.

3.5 Influence of microgravity on phase morphology

To study the influence of microgravity on the builds, two samples were built with the same manufacturing parameters and geometry—but differing gravity conditions. These samples were already introduced in a previous paper [19]. A scanning electron micrograph of each sample is shown in Fig. 9. The µg-sample presents more balling, which can be understood by the reduced hydrostatic pressure on the melted metals due to weightlessness, particularly at the ends of individual lines. The lab sample is smoother in appearance.

In terms of phase analysis, both samples were previously examined in the as-built condition in X-ray micro-diffraction [19]. From the diffraction results, no significant difference is observed in the diffraction patterns of both the µg- and lab sample. Because the X-ray diffraction experiment could not reveal more details in terms of higher resolution due to the limited thickness of the samples, additional investigations were performed employing TEM. TEM microstructure analysis obtained from the MAPHEUS-10 µg-sample and the corresponding lab equivalent of AMLOY-Zr01 is shown in Fig. 10. The TEM samples were taken from the interlayer regions between two building layers. Clusters of nanocrystalline phases with spherical or ellipsoidal morphology have been observed, as shown in Fig. 10a and Fig. 10c for the µg and lab sample, respectively. These clusters exhibit clearly defined phase boundaries to the amorphous matrix, as confirmed by the distinct diffraction spots next to the amorphous ring in the corresponding SAED patterns in Fig. 10b and Fig. 10d. No quasi-crystalline structures have been observed.

Average sizes of the nanocrystalline phases in this region are given in Table 4. Smaller sizes of the phases are measured in the µg-sample compared to the lab equivalent. This could be attributed to the fact that the outer temperature of the entire MARS-M payload at launch was low (below 300 K due to the weather conditions), so that at least part of the processing were performed during which the temperature of the base plate was also lower than that under laboratory conditions. However, considering the fact that TEM only samples a small fraction of the sample, this could be only one of the possible reasons, and we do not exclude other potential effects. Also, the base plate was warmed up by the heating laser as the AM proceeded. Thus, this impact is expected to diminish.

HRTEM-BF images, as shown in Fig. 11, were taken from the spherical and ellipsoidal particles in the

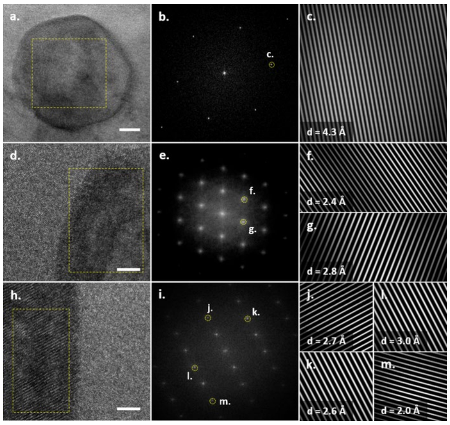

Fig. 11 HRTEM-BF micrographs and corresponding FFT and IFFT processed images of the marked region of MAPHEUS-10 lab equivalent (a.-c.) and flight sample (d.-m) at the interface of two layers. The scale bar of HRTEM images is 20 nm (a.) and 5 nm (d.,h.)

µg-sample and in the lab equivalent. Figure 11a shows a HRTEM image of a spherical particle in the lab sample. The corresponding FFT and inverse FFT processed HRTEM images, shown in Fig. 11b and Fig. 11c, respectively, reveal an FCC structure with an average d-spacing of 4.354 ± 0.533Å (Fig. 11c). Since the zone axis of the pattern is clearly $[\bar{1}11]$, the diffraction spots close to it therefore belong to {220} plane family [43], and an average lattice parameter of 12.284±0.152Å is derived, which fits at best to Cu_2Zr_4O [27, 30, 44–47].

In the literature, a wide range of lattice parameters from 11.9–12.28Å is reported for the Cu_2Zr_4O phase [27, 30, 44–48], as a large amount of Al can be dissolved in Cu_2Zr_4O [34] and it is assumed that Al substitutes Zr in its lattice sites. Furthermore, it is also possible that Al substitutes Cu to some extent as proposed by Tidefelt et al., forming $(Al,Cu)Zr_2$ and $(Al,Cu)_3Zr_4$ phases [32]. Due to the larger atomic radius of Al compared to Cu, such substitution could lead to additional increases of the lattice constant [49]. With respect to the EDS maps in Fig. 12, the crystalline regions are enriched with Al and O. Therefore, it is reasonable that the derived lattice constant here is closer to the upper limit of the range reported in the literature [30, 46].

HRTEM images of ellipsoidal particles in the µg-sample are shown in Fig. 11d and Fig. 11h. The corresponding FFT processed images reveal either an FCC structure (Fig. 11e-Fig. 11g) or a hexagonal structure (Fig. 11i-Fig. 11m). The pattern of the FCC structure (Fig. 11e) is oriented in the [011] zone axis with diffraction reflections close to zone axis belonging to {111} and {200} plane family. Based on this, the lattice parameter is determined to be 5.458 ± 0.160Å, which is close to the lattice parameter a of hexagonal Al_3Zr_4. However, none of the so far reported cubic phases fits to this lattice parameter. Concerning the chemical composition of the phase, no significant difference compared to the spherical cubic Cu_2Zr_4O phase has been observed.

The crystalline structure (shown in Fig. 11h) could be related to a hexagonal structure oriented in $[2\bar{1}\bar{1}0]$ zone axis as visible in Fig. 11i-Fig. 11m, based on the perfectly matching angle and distance relationship of visible diffraction reflections. In this case, the measured d-spacing of the (0002) reflection (Fig. 11j) is about 2.696 ± 0.040Å, which results in a lattice parameter of 5.393 ± 0.081Å. This value is in good agreement with the lattice parameter c of Al_3Zr_4 reported in the literature [50]. This is also valid for the (0001) reflection that appears due to double diffraction.

However, other d-spacings measured from reflections at $(01\bar{1}0)$, $(01\bar{1}1)$ or $(01\bar{1}2)$ positions and the calculated lattice parameters of 3.446 ± 0.015Å do not correspond to the lattice parameter a of the hexagonal Al_3Zr_4 phase [50]. In view of these results, both structures observed in the ellipsoidal particles could correspond to transition states between Cu_2Zr_4O and $(Al,Cu)_3Zr_4$ due to their

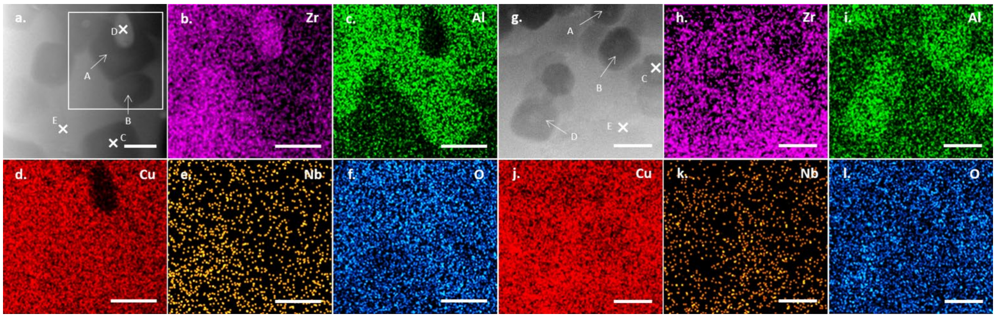

Fig. 12 EDS maps of crystalline phases in the interface region of MAPHEUS-10 µg-sample (a.-f.) and lab equivalent (g.-l.) of AMLOY-Zr01. EDS maps of µg-sample refer to the marked rectangular area in a. and scale bar represents 100 nm. Capital letters refer to local chemical composition given in Table 5

Table 5 Chemical composition of nanocrystalline phases and amorphous region next to it obtained from EDS spectra of the μg-sample with respect to location A–E in Fig. 12a in at.%, as well as chemical composition of nanocrystalline phases obtained from EDS spectra of lab equivalent with respect to location A–E in Fig. 12g in at.%

flight sample					
Element	A	B	C	D	E
O	13.97	13.64	14.02	18.84	10.29
Al	12.39	10.05	12.81	2.65	4.45
Cu	33.36	33.15	33.32	18.63	33.07
Zr	39.97	39.98	40.18	59.31	50.94
Nb	0.99	1.19	0.68	0.57	1.26
lab equivalent					
Element	A	B	C	D	E
O	18.46	18.27	17.78	16.43	10.41
Al	13.09	15.64	13.18	15.62	9.76
Cu	31.18	32.05	31.10	32.86	29.27
Zr	36.79	33.88	37.55	34.89	49.22
Nb	0.49	0.16	0.40	0.21	1.34

lattice parameter 5.458 ± 0.160Å being partially close to the lattice parameters *a* and *c* reported for Al_3Zr_4, and their chemical composition being comparable to Cu_2Zr_4O [46, 50, 51]. However, the possibility of a so far unknown phase cannot be completely ruled out.

The EDS element maps of the nanocrystalline phases and the surrounding nearby amorphous matrix for the μg-sample and the lab equivalent are shown in Fig. 12. The corresponding EDS results of the highlighted crystalline and amorphous regions are presented in Table 5.

With respect to the nominal chemical composition of AMLOY-Zr01, nanocrystalline phases are depleted in Zr, but are enriched in Al and slightly in Cu, which agrees with the previous reports on the cubic phase Cu_2Zr_4O [34, 46]. In the μg-sample, the amorphous matrix in the close vicinity of nanocrystalline phases is either slightly depleted in Al and Zr or depleted in Cu (Table 5 D, E) compared to the chemical composition of AMLOY-Zr01. An Al and Zr depletion of the amorphous matrix is also measured in the lab equivalent (Table 5 E). In general, the chemical composition determined by EDS is similar to what de Olivera et al. [46] have measured for Cu_2Zr_4O and its surrounding amorphous matrix. Slightly more oxygen has been detected in the crystalline phases of the lab equivalent compared to the μg-sample. However, a nominal difference in oxygen content between the experiments cannot be fully disregarded. The Nb content is in general much lower than expected from the nominal chemical composition of AMLOY-Zr01. With regards to the phases present as a function of gravity, no difference is observed on the basis of the TEM analysis.

The characterization of the nanocrystalline phases by their stoichiometric compositions using TEM-EDS was not possible due to their size and signal overlap with the surrounding bulk matrix. Furthermore, it is possible that the TEM analysis does not identify all existing phases, since only small sections can be analyzed. Nevertheless, the EDS results revealed significant Al incorporation in the Cu_2Zr_4O phase, which is believed to be responsible for the increased lattice constant derived from HRTEM. Moreover, the identification of the Cu_2Zr_4O phase by both TEM and SEM, and in particular the presence of a transition state between Cu_2Zr_4O and $(Al,Cu)_3Zr_4$, indicates that the formation of the both phases could be related, despite the potentially different cooling rates. Especially, the observed more volumetric distribution of Al_3Zr_4 in the bulk sample by XRD-CT may be a result of triggered formation of the Al_3Zr_4 phase by the nucleation of Cu_2Zr_4O in the melt, either due to heterogeneous nucleation or due to a remaining liquid depleted in $CuZr_2$

4 Conclusion and outlook

To summarize, using the MARS-M device, samples of AMLOY-Zr01 metallic glass compositions were built in the lab and in microgravity. Extensive analysis of both gravity states revealed complex crystalline phases among an amorphous matrix for all samples, whose fraction depends on the process parameters, in this case laser power and scanning speed used. The minimum laser powers necessary to produce samples without large pores are similar to that used in the conventional LPBF processes [27]. Also, the trend that the crystalline fraction increases with increasing laser power agrees with the observation in LPBF-processed of BMGs without a gas flow. Therefore, the technique is considered to be suited for both ground and space applications.

No significant difference – beyond the physical outer aspect – is observed between the part built in microgravity and that built in the lab. Thus, it is concluded that using the gas flow-assisted mechanism for stabilizing the powder bed, similar process conditions as the conventional LPBF can be established. Thus, the current knowledge on optimizing the process parameters for AM of BMGs can be transferred. Differences between samples processed in microgravity and on ground are mainly originated from the wetting behavior of the melt. This is an interplay between surface tension and hydrostatic pressure generated by the gas flow, which remains to be further explored for longer microgravity time, and compared with other AM approaches. One might expect convection to make a difference, as it is a parameter shown to affect the phase formation from the melt [52, 53]. However, as the cooling during LPBF is generally fast, and the viscosity of the glass forming alloys is relatively high [22], convection within the melt could be limited, whether in the lab or in microgravity.

This crystalline region is mostly present in the interlayer regions, as shown in SEM and in X-ray diffraction and tomography. Moreover, while the crystallization at the interface is known to associate with HAZ and therefore scanning strategy, the observed Al_3Zr_4 phase appears to show more volumetric distribution. It has been found that the formation of Al_3Zr_4 appears to be closely related to the nucleation of the Cu_2Zr_4O phase in the melt, and hence the oxygen content in the processes. Thus, in terms of manufacturing fully amorphous parts in space, higher scanning speeds and a reduced oxygen content are necessary. The current limit of the laser scanning speed can be overcame, e.g., for long-term missions, where the acceleration of the launch is lower or sensitive laser systems can be assembled after launch, while from the mechanical strength point of view, residual oxygen content and some crystalline fraction could provide even certain advantages. In particular, for AMLOY-Zr01, it has been shown that additively manufactured sample with higher oxygen content exhibits higher contact stiffness (more resistance to shear, also higher elastic modulus) but lower fracture toughness (more brittle) [54].

Supplementary Information The online version contains supplementary material available at https://doi.org/10.1007/s40964-025-01275-2.

Acknowledgements We thank the Esrange staff (SSC, Jukkasjärvi, Sweden) for their support, time and energy during the MAPHEUS sounding rocket campaigns. We acknowledge DESY (Hamburg, Germany), a member of the Helmholtz Association HGF, for the provision of experimental facilities. Parts of this research were carried out at PETRA III with beamtime allocated for proposal I-20221251. Data was collected at the P07 beamline operated by DESY Photon Science. We acknowledge the Smoothieware community. The authors would like to thank Dr. Maike Becker for a critical proof-reading of the manuscript and her valuable suggestions.

Author Contributions CN and JT designed and built the setup. CN, JT, MC, and JW ran measurements in the lab and during MAPHEUS campaigns. CN, JT, MC, and FY oversaw and guided measurements during the synchrotron beamtime. OG and ACD guided and performed the measurements during the synchrotron beamtime. OG processed the XRD-CT data including the reconstruction. LR and RB initiated and conducted the differential calorimetry measurements. MC and MK performed together the SEM studies and analyzed the results. CKA and CA conducted TEM investigations, analyzed, and interpreted the TEM results. MC and FY analyzed and interpreted the data. MC, FY, CN, and CA wrote the manuscript. DZ initiated and supported the TEM investigations. AM initiated and supported the project as well as procured the flight opportunities. All authors revised the manuscript.

Funding Open Access funding enabled and organized by Projekt DEAL.

Data Availability The datasets used and/or analyzed during the current study are available from the corresponding author on reasonable request.

Declarations

Conflict of interest The authors declare no conflict of interest.

References

1. Ashby M, Greer AL (2006) Metallic glasses as structural materials. Scr Mater 54(3):321–326. https://doi.org/10.1016/j.scriptamat.2005.09.051
2. Kruzic JJ (2016) Bulk metallic glasses as structural materials: a review. Adv Eng Mater 18(8):1308–1331. https://doi.org/10.1002/adem.201600066
3. Greer AL, Ma E (2007) Bulk metallic glasses: at the cutting edge of metals research. MRS Bull 32(8):611–619. https://doi.org/10.1557/mrs2007.121
4. Williams E, Lavery N (2017) Laser processing of bulk metallic glass: a review. J Mater Proc Technol 247:73–91. https://doi.org/10.1016/j.jmatprotec.2017.03.034
5. Best JP, Ostergaard HE, Li B, Stolpe M, Yang F, Nomoto K, Hasib MT, Muránsky O, Busch R, Li X, Kruzic JJ (2020) Fracture and fatigue behaviour of a laser additive manufactured Zr-based bulk metallic glass. Addit Manuf 36:101416. https://doi.org/10.1016/j.addma.2020.101416
6. Sohrabi N, Jhabvala J, Logé RE (2021) Additive manufacturing of bulk metallic glasses − process. Challenges and properties a review. Metals 11(8):1279. https://doi.org/10.3390/met11081279
7. Gibson I, Rosen D, Stucker B (2015) Additive manufacturing technologies. Springer, New York, NY
8. Gibson I, Rosen D, Stucker B, Khorasani M (eds) (2021) Additive manufacturing technologies. Springer International Publishing, Cham
9. Srivastava M, Rathee S, Patel V, Kumar A, Koppad PG (2022) A review of various materials for additive manufacturing: recent trends and processing issues. J Mater Res Technol 21:2612–2641. https://doi.org/10.1016/j.jmrt.2022.10.015
10. Herderick E (2011) Additive manufacturing of metals: a review. Proceedings of MS &T'11, additive manufacturing of metals
11. Sanchez S, Smith P, Xu Z, Gaspard G, Hyde CJ, Wits WW, Ashcroft IA, Chen H, Clare AT (2021) Powder bed fusion of nickel-based superalloys: a review. Int J Mach Tools Manuf 165:103729. https://doi.org/10.1016/j.ijmachtools.2021.103729
12. Zocca A, Colombo P, Gomes CM, Günster J (2015) Additive manufacturing of ceramics: issues, potentialities, and opportunities. J Am Ceram Soc 98(7):1983–2001. https://doi.org/10.1111/jace.13700
13. Goodridge R, Ziegelmeier S (2016) 7 Powder bed fusion of polymers. In: Brandt M (ed) Laser Additive Manufacturing. Woodhead publishing series in electronic and optical materials. Elsevier and

Woodhead Publishing, Amsterdam and Boston and Cambridge, pp 181–204

14. Kusoglu IM, Doñate-Buendía C, Barcikowski S, Gökce B (2021) Laser powder bed fusion of polymers: quantitative research direction indices. Materials 14(5):1169. https://doi.org/10.3390/ma14051169
15. Frazier WE (2014) Metal additive manufacturing: a review. J Mater Eng Perform 23(6):1917–1928. https://doi.org/10.1007/s11665-014-0958-z
16. Song B, Zhao X, Li S, Han C, Wei Q, Wen S, Liu J, Shi Y (2015) Differences in microstructure and properties between selective laser melting and traditional manufacturing for fabrication of metal parts: a review. Front Mech Eng 10(2):111–125. https://doi.org/10.1007/s11465-015-0341-2
17. Zocca A, Lüchtenborg J, Mühler T, Wilbig J, Mohr G, Villatte T, Léonard F, Nolze G, Sparenberg M, Melcher J, Hilgenberg K, Günster J (2019) Enabling the 3D printing of metal components in ţ-gravity. Adv Mater Techol 4(10):1900506. https://doi.org/10.1002/admt.201900506
18. Zocca A, Wilbig J, Waske A, Günster J, Widjaja MP, Neumann C, Clozel M, Meyer A, Ding J, Zhou Z, Tian X (2022) Challenges in the technology development for additive manufacturing in space. Chin J Mech Eng Addit Manuf Front 1(1):100018. https://doi.org/10.1016/j.cjmeam.2022.100018
19. Neumann C, Thore J, Clozel M, Günster J, Wilbig J, Meyer A (2023) Additive manufacturing of metallic glass from powder in space. NPJ microgravity 9(1):80. https://doi.org/10.1038/s41526-023-00327-7
20. Hofmann DC, Bordeenithikasem P, Tosi LP, Hendry M, Yahnker C, Sunday C, Pate A, Firdosy S, Iten JJ, Nuechterlein J, Stolpe M (2020) Towards additively manufacturing excavating tools for future robotic space exploration. Eng Rep 2(8):12219. https://doi.org/10.1002/eng2.12219
21. Heinrich J, Busch R, Nonnenmacher B (2012) Processing of a bulk metallic glass forming alloy based on industrial grade Zr. Intermetallics 25:1–4. https://doi.org/10.1016/j.intermet.2012.02.011
22. Jonas I, Hembree W, Yang F, Busch R, Meyer A (2018) Industrial grade versus scientific pure: influence on melt properties. Appl Phys Lett 112(17):171902. https://doi.org/10.1063/1.5021764
23. Ericsson A, Pacheco V, Marattukalam JJ, Dalgliesh RM, Rennie AR, Fisk M, Sahlberg M (2021) Crystallization of a Zr-based metallic glass produced by laser powder bed fusion and suction casting. J Non-Cryst Solids 571:120891. https://doi.org/10.1016/j.jnoncrysol.2021.120891
24. Günster J Personal communication (31.05.2023)
25. Schneider CA, Rasband WS, Eliceiri KW (2012) NIH Image to ImageJ: 25 years of image analysis. Nat Methods 9:671–675. https://doi.org/10.1038/nmeth.2089
26. Kieffer J, Karkoulis D (2013) pyFAI, a versatile library for azimuthal regrouping. J Phys: Conf Ser 425(20):202012. https://doi.org/10.1088/1742-6596/425/20/202012
27. Marattukalam JJ, Pacheco V, Karlsson D, Riekehr L, Lindwall J, Forsberg F, Jansson U, Sahlberg M, Hjörvarsson B (2020) Development of process parameters for selective laser melting of a Zr-based bulk metallic glass. Addit Manuf 33:101124. https://doi.org/10.1016/j.addma.2020.101124
28. Sohrabi N, Jhabvala J, Kurtuldu G, Stoica M, Parrilli A, Berns S, Polatidis E, van Petegem S, Hugon S, Neels A, Löffler JF, Logé RE (2021) Characterization, mechanical properties and dimensional accuracy of a Zr-based bulk metallic glass manufactured via laser powder-bed fusion. Mater Des 199:109400. https://doi.org/10.1016/j.matdes.2020.109400
29. Kawase D, Tsai AP, Inoue A, Masumoto T (1993) Crystallization on supercooled liquid in metallic ZrCuAl glasses. Appl Phys Lett 62(2):137–139. https://doi.org/10.1063/1.109350
30. Pacheco V, Karlsson D, Marattukalam JJ, Stolpe M, Hjörvarsson B, Jansson U, Sahlberg M (2020) Thermal stability and crystallization of a zr-based metallic glass produced by suction casting and selective laser melting. J Alloys Compd 825:153995. https://doi.org/10.1016/j.jallcom.2020.153995
31. Qiang JB, Zhang W, Xie GQ, Inoue A (2007) The effect of Ti, Nb, and Ta additions to ZrAlCu metallic glass on the crystallization and formation of the icosahedral phase. J Mater Res 22(4):1093–1097. https://doi.org/10.1557/jmr.2007.0130
32. Tidefelt M, Löfstrand J, Goetz IK, Donzel-Gargand O, Ericsson A, Han X, Jönsson PE, Sahlberg M, Kaban I, Fisk M (2024) In situ mapping of phase evolutions in rapidly heated Zr-based bulk metallic glass with oxygen impurities. Adv Sci 11(2307856):1–13. https://doi.org/10.1002/advs.202307856
33. Wegner J, Frey M, Piechotta M, Neuber N, Adam B, Platt S, Ruschel L, Schnell N, Riegler SS, Jiang H-R, Witt G, Busch R, Kleszczynski S (2021) Influence of powder characteristics on the structural and the mechanical properties of additively manufactured Zr-based bulk metallic glass. Mater Des 209:109976. https://doi.org/10.1016/j.matdes.2021.109976
34. Yang Z, Wang H, Krauß S, Huber F, Merle B, Schmidt M, Markl M, Körner C (2022) Evolution of an industrial-grade Zr-based bulk metallic glass during multiple laser beam melting. J Non-Cryst Solids 589:121649. https://doi.org/10.1016/j.jnoncrysol.2022.121649
35. Sohrabi N, Panikar RS, Jhabvala J, Buch AR, Mischler S, Logé RE (2020) Laser coating of a Zr-based metallic glass on an aluminum substrate. Surf Coat Technol 400:126223. https://doi.org/10.1016/j.surfcoat.2020.126223
36. Shen Y, Li Y, Tsai H-L (2018) Evolution of crystalline phase during laser processing of Zr-based metallic glass. J Non-Cryst Solids 481:299–305. https://doi.org/10.1016/j.jnoncrysol.2017.11.001
37. Di O, Li N, Xing W, Zhang J, Liu L (2017) 3D printing of crack-free high strength Zr-based bulk metallic glass composite by selective laser melting. Intermetallics 90:128–134. https://doi.org/10.1016/j.intermet.2017.07.010
38. Li XP, Roberts MP, O'Keeffe S, Sercombe TB (2016) Selective laser melting of Zr-based bulk metallic glasses: processing, microstructure and mechanical properties. Mater Des 112:217–226. https://doi.org/10.1016/j.matdes.2016.09.071
39. Zhang Y, Lin X, Wang L, Wei L, Liu F, Huang W (2015) Microstructural analysis of Zr$_{55}$Cu$_{30}$Al$_{10}$Ni$_{5}$ bulk metallic glasses by laser surface remelting and laser solid forming. Intermetallics 66:22–30. https://doi.org/10.1016/j.intermet.2015.06.007
40. Yang G, Lin X, Liu F, Hu Q, Ma L, Li J, Huang W (2012) Laser solid forming Zr-based bulk metallic glass. Intermetallics 22:110–115. https://doi.org/10.1016/j.intermet.2011.10.008
41. Yang Z, Wang H, Krauß S, Huber F, Merle B, Schmidt M, Markl M, Körner C (2022) Evolution of an industrial-grade Zr-based bulk metallic glass during multiple laser beam melting. J Non-Cryst Solids 589:121649. https://doi.org/10.1016/j.jnoncrysol.2022.121649
42. Nolze G, Tokarski T, Rychłowski Ł, Cios G, Winkelmann A (2021) Crystallographic analysis of the lattice metric (CALM) from single electron backscatter diffraction or transmission kikuchi diffraction patterns. J Appl Crystallogr 54(3):1012–1022. https://doi.org/10.1107/S1600576721004210
43. Andersen LM (2016) Toughness of wear-resistant Cu-Zr-based bulk metallic glasses. University of California, San Diego
44. Goetz IK, Pacheco V, Hassila CJ, Jansson U, Schneider JM, Hans M (2023) Convective flow redistribution of oxygen by laser

melting of a zr-based amorphous alloy. Materials 16(11):4113. https://doi.org/10.3390/ma16114113

45. Mackay R, Miller GJ, Franzen HF (1994) New oxides of the filled-Ti_2Ni type structure. J Alloys Compd 204(1):109–118. https://doi.org/10.1016/0925-8388(94)90079-5
46. Oliveira Md, Kaufman MJ, Botta Filho WJ, Kiminami CS (2002) The "Big-Cube'' phase found in Zr-Cu-Al-Ni easy glass forming alloys. J Metastab Nanocryst Mater 14:101–106. https://doi.org/10.4028/www.scientific.net/JMNM.14.101
47. Yan M, Zou J, Shen J (2006) Cooling rate effects on the microstructure and phase formation in $Zr_{51}Cu_{20.7}Ni_{12}Al_{16.3}$ bulk metallic glass. Sci Technol Adv Mater 7(8):806. https://doi.org/10.1016/j.stam.2006.11.009
48. Sviridova T, D'yakonova N, Shelekhov E, Glazkov V (2004) Change of crystal structure of Zr_2Cu after a treatment in ball mill and annealing. Poverkhnost'. Rentgenovskie, Sinkhrotronnye i Nejtronnye Issledovaniya, 28–32
49. Takeuchi A, Inoue A (2005) Classification of bulk metallic glasses by atomic size difference, heat of mixing and period of constituent elements and its application to characterization of the main alloying element. Mater Trans 46(12):2817–2829. https://doi.org/10.2320/matertrans.46.2817
50. Wilson C, Thomas D, Spooner F (1960) The crystal structure of Zr_4Al_3. Acta Crystallogr 13(1):56–57. https://doi.org/10.1107/S0365110X60000121
51. Wilson CG, Wilson N, Joksimovic V, Westphalen JA (1973) The effect of fast-neutron irradiation on Zr_4Al_3. Acta Cryst A 29(4):336–341. https://doi.org/10.1107/S0567739473000926
52. Becker M, Wegener M, Drescher J, Kargl F (2023) Nucleation and growth dynamics of equiaxed dendrites in thin metallic Al-Cu and Al-Ge samples in microgravity and on earth. Metall Mater Trans A 54(11):4188–4202. https://doi.org/10.1007/s11661-023-07079-9
53. Nguyen-Thi H, Reinhart G, Billia B (2017) On the interest of microgravity experimentation for studying convective effects during the directional solidification of metal alloys. Comptes Rendus Mécanique 345(1):66–77. https://doi.org/10.1016/j.crme.2016.10.007
54. Best JP, Ast J, Li B, Stolpe M, Busch R, Yang F, Li X, Michler J, Kruzic JJ (2020) Relating fracture toughness to micro-pillar compression response for a laser powder bed additive manufactured bulk metallic glass. Mater Sci Eng, A 770:138535. https://doi.org/10.1016/j.msea.2019.138535

Authors and Affiliations

Melanie Clozel[1] · Christian Neumann[1] · Johannes Thore[1] · Matthias Kolbe[1] · Fan Yang[1] · Olof Gutowski[2] · Ann-Christin Dippel[2] · Lucas M. Ruschel[3] · Ralf Busch[3] · Christoph Altenbach[1] · Chijioke Kenneth Akuata[1,4] · Daniela Zander[1,4] · Janka Wilbig[5] · Andreas Meyer[1]

✉ Melanie Clozel
Melanie.Clozel@dlr.de

✉ Fan Yang
fan.yang@dlr.de

Christian Neumann
Christian.Neumann@dlr.de

Johannes Thore
Johannes.Thore@dlr.de

Matthias Kolbe
matthias.kolbe@dlr.de

Olof Gutowski
olof.gutowski@desy.de

Ann-Christin Dippel
ann-christin.dippel@desy.de

Lucas M. Ruschel
lucas.ruschel@uni-saarland.de

Ralf Busch
r.busch@mx.uni-saarland.de

Christoph Altenbach
christoph.altenbach@dlr.de

Chijioke Kenneth Akuata
chijioke.akuata@dlr.de

Daniela Zander
daniela.zander@dlr.de

Janka Wilbig
janka.wilbig@lne.fr

Andreas Meyer
meyera@ill.fr

[1] Institut für Materialphysik im Weltraum, Deutsches Zentrum für Luftund Raumfahrt (DLR), 51170 Cologne, Germany

[2] Deutsches Elektronen-Synchrotron DESY, 22607 Hamburg, Germany

[3] Lehrstuhl für Metallische Werkstoffe, Universität des Saarlandes, 66123 Saarbrücken, Germany

[4] Lehrstuhl für Korrosion und Korrosionsschutz, Gießerei Institut, Fachgruppe Materialwissenschaft und Werkstofftechnik, RWTH Aachen, 52072 Aachen, Germany

[5] Bundesanstalt für Materialforschung und -prüfung (BAM), 12205 Berlin, Germany